https://doi.org/10.5194/essd-2026-21
Preprint. Discussion started: 9 February 2026

Open Access Earth System Science Data Discussions

Finer-Resolution Long-Term Mapping of Plant Functional Types at 30-m Resolution and Corresponding Leaf Area Index for Earth System Modeling

Wanyi Lin[1,2], Hua Yuan[1], Wenzong Dong[1], Zhuo Liu[1], Jiayi Xiang[1], Xinran Yu[1], Shupeng Zhang[1], Zhongwang Wei[1], Yongjiu Dai[1]

[1]School of Atmospheric Sciences, Sun Yat-sen University, Zhuhai, 519082, China
[2]Guangzhou Meteorological Satellite Ground Station (Guangdong Meteorological Satellite Remote Sensing Centre), Guangzhou, 510640, China

Correspondence to: Hua Yuan (yuanh25@mail.sysu.edu.cn)

Abstract. Land surface data describe the heterogeneity of the terrestrial surface and serve as fundamental input for earth system models. Under ongoing climate change and increasing intensity of human activities, land surface data are required to quantify the impact of land use and land cover change (LULCC) and their contribution to regional and global climate. Plant functional type (PFT) and PFT-specific leaf area index (PFT LAI) characterize land surface and vegetation canopy attributes and are essential model inputs. However, uncertainties associated with current derivation methods may limit their application in earth system models. Moreover, long-term, high-resolution datasets of PFT distributions and PFT LAI remain scarce for fine-scale simulations. To address these gaps, we derived a global 30 m PFT map (PFT30) spanning 1985–2020, updated at five-year intervals prior to 2000 and annually thereafter. By integrating multiple high-resolution remote sensing products, we minimized the assumptions typically required for PFT fraction determination. Building on PFT30, we generated a monthly 500 m PFT LAI dataset for 1985–2020 by fusing PFT30 with the reprocessed MODIS C6.1 LAI and GIMMS LAI4g products, using a remote-sensing-derived phenology scheme instead of the empirical approaches commonly adopted in land surface models. Comparisons with three other hundred-meter global PFT products show that all datasets produce broadly consistent tree fractions, while short-vegetation fractions differ substantially; PFT30 shows better agreement with site observations. Compared with empirical schemes, the new PFT LAI dataset can better distinguish short vegetation types such as grasses, shrubs and crops, because it captures realistic phenological variations directly from remote sensing. This long-term, high-resolution PFT map and the associated PFT LAI data provide a finer representation of land surface characteristics and can be applied in land surface and earth system modeling from regional to global scales.

1 Introduction

Land surface data is one of the basic input components of earth system models (ESMs), providing essential information on surface attributes. Given the strong heterogeneity of the land surface, accurately representing its characteristics is crucial for

https://doi.org/10.5194/essd-2026-21
Preprint. Discussion started: 9 February 2026

improving the simulation of state variables and land-atmosphere fluxes (Fisher and Koven, 2020). With the continuous development of land surface and climate models toward higher spatial resolutions (Wu et al., 2025), from tens of kilometers to kilometer or even sub-kilometer scales, the demand for land surface datasets with higher spatial and temporal fidelity has increased substantially. High-resolution land surface data can more accurately characterize surface heterogeneity and vegetation composition, thereby improving the representation of energy, water, and carbon fluxes and enhancing the simulation of related processes (Jian et al., 2025; Malle et al., 2024). Meanwhile, human activities such as agricultural expansion, grazing, urbanization, and deforestation have caused extensive changes to the natural land surface. By 2015, more than 70% of the non-ice land area had been directly used by humans, and one-third of this area had experienced land cover transitions (IPCC, 2022). Such changes alter land surface attributes, including surface roughness, albedo and evapotranspiration processes, influencing both biogeophysical and biogeochemical processes (Betts, 2000; Boysen et al., 2014; Winckler et al., 2019; Zeng et al., 2018), and may ultimately affect regional and global climate. Therefore, land surface data with high accuracy and fine spatial resolution is essential for quantifying the impacts of historical and present LULCC.

Some land surface models (LSMs) used to describe land vegetation as discrete land cover types (LCT) and used a set of consistent parameters for mixed lifeforms ecosystem. As a result, this representation fails to capture the leaf-level or plant-level physiological processes of different lifeforms, which further limits coupling with ecosystem dynamic models and biogeochemical models (Bonan et al., 2002). Moreover, the interannual variability in LCT products, particularly at medium to coarse spatial resolutions, may be obscured by classification uncertainties (Sulla-Menashe et al., 2019), potentially leading to biases in LULCC detection.

In contrast, plant functional types (PFT) classification can account for the continuous distribution and mixing of vegetation types (Smith et al., 1997), while coherently integrating vegetation physical processes, physiological processes, and ecological processes. Therefore, PFT has become widely adopted as sub-grid classification schemes in many LSMs, including CABLE (CSIRO Atmosphere Biosphere Land Exchange), CLM (Community Land Model), JULES (Global Land configuration of the Joint UK Land Environment Simulator) and JSBACH (Jena Scheme for Biosphere-Atmosphere Coupling in Hamburg), enabling more accurate parameterization of land surface vegetation.

PFT datasets derived from remote sensing products are generally generated using three main approaches. The simplest method is direct mapping between LCT labels and fixed PFT compositions, in which each LCT category is assigned to a single PFT or a predefined PFT mixture. For example, the PFT layer in the MODIS MCD12Q1 product is directly converted from its IGBP land cover classification (Sulla-Menashe et al., 2019) and has been adopted in previous studies (Ke et al., 2012; Li et al., 2024). However, this approach does not explicitly decompose LCT classes into sub-grid PFT fractions and therefore cannot realistically represent the actual PFT composition within a pixel. Compared with the direct LCT-PFT mapping approach, the look-up table approach provides a better representation of sub-grid surface heterogeneity and has been widely adopted (Faroux et al., 2013; Houldcroft et al., 2009; Poulter et al., 2011, 2015; Wang et al., 2023). This method interprets LCT class labels

https://doi.org/10.5194/essd-2026-21
Preprint. Discussion started: 9 February 2026

and converts each class into fractional compositions of multiple PFTs based on predefined rules. For example, the ESA Climate Change Initiative (ESA-CCI) PFT product is generated from the 300 m LC_CCI land cover dataset using an expert-based cross-walking scheme to translate LCT classes into PFT fractions (Poulter et al., 2015). As this approach relies on indirect inference from LCT labels, its reliability depends on both the roubustness of the cross-walking rules and the classification accuracy of the underlying LCT product. Consequently, it still has limitations in realistically representing true vegetation composition, especially in ecotones and mixed-pixel regions. To better represent spatial heterogeneity, some studies have introduced multi-source remote sensing products to directly constrain the distribution of specific PFTs (Bonan et al., 2002; Lawrence and Chase, 2007). For example, recent efforts have improved the ESA-CCI global 300 m PFT dataset by incorporating high-resolution auxiliary products (Harper et al., 2023). Although this approach enhances the spatial representation of regional PFT composition, some uncertainty remains due to the reliance on LCT-based assumptions in determining PFT fractions. Moreover, the uncertainty in PFT distribution based on LCT data has been shown to be comparable to the uncertainty among different model simulations (Hartley et al., 2017).

While PFT distribution provides sub-grid vegetation fractional coverage, accurate simulation of vegetation processes in LSMs also requires leaf area index (LAI). As a key parameter describing the canopy structure and physiology of vegetation, LAI substantially affects radiative transfer, precipitation interception, turbulent exchange, as well as photosynthesis and respiration. Long-term LAI records are essential for analyzing vegetation dynamics and global greening trends (Chen et al., 2019; Xie et al., 2022). Although many grid-scale LAI products are available from remote sensing, ecosystem models, or machine learning, they cannot be directly applied in PFT-based modeling and must be converted into PFT-specific LAI (hereafter PFT LAI).

Current research on deriving PFT LAI remains limited, and existing methods are subject to considerable uncertainty. Two main approaches are commonly used: (1) simulating vegetation physiological processes under environmental drivers via dynamic vegetation models, and (2) allocating grid-scale LAI from satellites to different PFTs using empirical methods. For example, CLM employs an empirical phenology scheme based on climatological air temperature (Lawrence and Chase, 2007), while JULES assigns a “balanced” LAI for each PFT, representing the equilibrium between leaf growth and senescence, for distributing grid-scale LAI among PFTs (Wiltshire et al., 2020). However, these approaches do not adequately capture differences in LAI among PFTs and cannot fully reflect seasonal dynamics or management effects. Therefore, leveraging remote sensing data to derive PFT LAI is essential for reducing uncertainty and improving vegetation representation in land surface models.

In summary, although land surface models have increasingly adopted PFT-based representations to better describe vegetation composition, uncertainties in existing PFT derivation approaches have limited the availability of high-resolution, long-term PFT datasets suitable for model applications. Similarly, existing PFT LAI data are limited and subject to considerable uncertainty. To address this gap, this study develops a 30 m PFT distribution product (PFT30) and a corresponding PFT LAI dataset for 1985–2020 by integrating multiple remote-sensing products. The PFT30 dataset was generated using the land-cover

https://doi.org/10.5194/essd-2026-21
Preprint. Discussion started: 9 February 2026

dynamic monitoring dataset GLC_FCS30D, the Global Forest Cover Change (GFCC) dataset, MODIS Vegetation Continuous Fields (VCF) and other ancillary sources (Sect. 2.2.1). The PFT LAI was subsequently derived from the reprocessed MODIS Collection 6.1 (C6.1) LAI product using a remote-sensing-based phenology scheme (Sect. 2.2.2). The PFT30 dataset was then compared with several existing global PFT products (Sect. 3.2) and validated against site-level observations (Sect. 3.3). The PFT LAI data were further evaluated through comparison with PFT LAI derived from an empirical phenology scheme (Sect 3.4). In addition, the PFT LAI together with the PFT30 dataset were evaluated over the Amazon rainforest against traditional LCT data (Sect 3.5). Together, these efforts provide a high-resolution, long-term representation of land surface characteristics to support improved land surface and climate modeling.

2 Data and Methodology

2.1 Data used and purpose

The input datasets were listed in Table 1 and, with their descriptions provided in the following sections. To derive the global 30 m long-term PFT30 dataset and the 500 m PFT LAI dataset, we prioritized source datasets with the highest possible spatial resolution, the longest possible temporal coverage, and the best available product quality.

Table 1. Datasets used for deriving the PFT30 and PFT LAI products.

Dataset	Description	Year	Resolution	Frequency	Reference
GLC_FCS30D	Global 30 m surface coverage fine classification products	1985–2022	30 m	1985–1999: every 5 years，2000–2022: annually	Zhang et al., 2024
GFCC	Global 30 m Multi-Year Tree Cover	2000–2015	30 m	5 years	Townshend, 2016
MODIS VCF	MODIS Vegetation Continuous Fields product, Version 6 (MOD44B)	2000–2021	250 m	annual	DiMiceli et al., 2015
Köppen-Geiger climate classification	Present Köppen-Geiger climate classification maps at 1 km resolution	present	1 km	/	Beck et al., 2018

https://doi.org/10.5194/essd-2026-21
Preprint. Discussion started: 9 February 2026

WorldClim Version2	New 1 km spatial resolution climate surfaces for global land areas	/	1 km	monthly	Fick and Hijmans, 2017
Reprocessed MODIS v6.1 LAI	Reprocessed MODIS leaf area index produces, Version 6.1	2000–2023	500 m	8 days / monthly	Lin et al., 2023
GIMMS LAI4g	A global dataset of the GIMMS Leaf Area Index	1982–2020	1/12°	half month	Cao et al., 2023

2.1.1 Land cover product (30 m)

The GLC_FCS30D (Zhang et al., 2024) land cover product is used to distinguish vegetated classes from non-vegetated land types, including urban areas, water bodies, wetlands and glaciers. Also, it is used to determine the type of different lifeforms (phenology, leaf type), as described in Section 2.2.1. GLC_FCS30D can be reached at https://doi.org/10.5281/zenodo.8239305. It is developed from a full-time series of Landsat images and a continuous change detection model based on the Google Earth Engine (GEE) platform. This dynamic dataset contains 35 subcategories and demonstrates clear advantages in identifying forest and wetland types, with an overall accuracy of 80.88% across the ten major land cover classes. It updates annually after 2000 and at five-year intervals prior to 2000, covering 1985–2022 at 26 temporal snapshots, and meets this study's requirements for high spatial resolution and long-term coverage.

2.1.2 Tree cover product (30 m)

The GFCC product (Townshend, 2016) is used to determine the tree cover fraction in the 30 m grid. It can be downloaded at https://lpdaac.usgs.gov/products/gfcc30tcv003/. It is derived from the GFCC Surface Reflectance product (http://dx.doi.org/10.5067/MEaSUREs/GFCC/GFCC30SR.001) which is based on the enhanced Global Land Survey (GLS) datasets. The GFCC tree cover product provides 30 m resolution data for four reference periods centered on the years 2000, 2005, 2010, and 2015. This dataset, with its high overall accuracy (91%), global multi-temporal coverage, and continuous tree cover fraction, aligns well with the requirements of this study. In this study, for each target year, the GFCC tree cover dataset from the temporally closest reference year was adopted, following a nearest-year assignment strategy. As GFCC data are only available up to 2015, the 2015 tree cover product was used for all subsequent years through 2020.

2.1.3 The Vegetation Continuous Fields (VCF) product (250 m)

The MODIS VCF product (DiMiceli et al., 2015) provides annual estimates of fractional tree cover, non-tree vegetation cover, and bare soil cover at a 250 m resolution. In addition to its stable annual updates, the product offers sub-pixel quantification together with long-term global temporal continuity, enabling a more detailed representation of fractional land surface

https://doi.org/10.5194/essd-2026-21
Preprint. Discussion started: 9 February 2026

components. These characteristics make it particularly suitable for deriving bare soil coverage in this study. The dataset is available at https://doi.org/10.5067/MODIS/MOD44B.006.

2.1.4 The Köppen-Geiger climate zone product (1 km)

The present-day Köppen-Geiger climate classification map (Beck et al., 2018) is used to attach climate zone information to PFT categories. It is developed based on an ensemble of four high-resolution, topographically corrected climatic maps, and can be accessed via http://www.gloh2o.org/koppen. This widely used product captures global climate distribution patterns at a relatively high spatial resolution, making it suitable for matching analyses with high-resolution land surface data. The Köppen-Geiger system contains five main classes and 30 sub-classes of climate zones, which are determined by their monthly air temperature and precipitation.

2.1.5 The WorldClim Version2 product (1 km)

The 1 km WorldClim Version2 product (Fick and Hijmans, 2017) is used to determine the photosynthetic pathways (e.g. C_3 and C_4) of grass PFT based on the climatology monthly precipitation and temperature. This product, created from data collected at between 9000 and 60000 weather stations and aggregated over the period 1970–2000, facilitates the identification vegetation physiological traits and functions.

2.1.6 The reprocessed MODIS LAI product (500 m)

The reprocessed MODIS LAI product (Lin et al., 2023) is used for the calculation of PFT LAI. It is freely available via http://globalchange.bnu.edu.cn/research/laiv061. This product provides LAI data covering the period 2000–2023 at 500 m resolution with 8-day or monthly temporal resolution. The raw data used include the MODIS LAI C6.1 products MCD15A2H (Myneni et al., 2021a), MOD15A2H (Myneni et al., 2021b) and MODIS LCT product MCD12Q1 (Friedl and Sulla-Menashe, 2022). The reprocessed LAI product is developed based on a two-step integrated method (Yuan et al., 2011) and it validation against multiple reference map datasets shows better performance than the original product.

2.1.7 The GIMMS LAI4g product (1/12 degree)

The GIMMS LAI4g product (Cao et al., 2023) is also used for the calculation of PFT LAI. This half-month 1/12° product is developed for the period 1992–2002 using the Back Propagation Neural Network (BPNN) and a data consolidation method. It can be accessed at https://doi.org/10.5281/zenodo.7649108. Since the derivation of the GIMMS LAI4g product employed the reprocessed MODIS LAI product (2001–2020) to extend temporal coverage, LAI4g can be used to complement the lack of LAI data prior to 2000, allowing the two datasets to be combined into a continuous long-term LAI record.

https://doi.org/10.5194/essd-2026-21
Preprint. Discussion started: 9 February 2026


Open Access Earth System Science Data Discussions

2.2 Methodology

2.2.1 PFT fractional cover mapping

The PFT30 dataset consists of annual PFT distributions for 1985–2020, updated every five years prior to 2000, and was produced by integrating subgrid vegetation fractions, land cover information, and climate-informed allocation rules using multiple ancillary datasets with spatial resolutions ranging from tens to hundreds of meters (Sect. 2.1). For ancillary datasets with coarser spatial resolution than 30 m, values were assigned to each target 30 m grid cell based on the corresponding coarse-resolution grid in which it was located. The overall workflow is illustrated in Fig. 1 and consists of the following steps:

1. The percentage cover of five main types was calculated, including tree, shrub, natural grass, crop and bare soil. The percentage of tree was determined by the GFCC tree cover data, and the percentage of bare soil was directly adopted from the 250 m MODIS VCF data. To ensure consistency, tree cover was treated as the primary constraint, and bare soil fraction was limited to the residual area not occupied by trees. Crop PFT fraction is seen as the vegetated area in the grid if the target grid was classified as crop LCT, therefore its fraction is assigned as the remaining fraction of bare cover.

2. The remaining percentage, after accounting for tree and bare soil, was assigned to shrub or grass PFT when the grid was classified as shrub or grass LCT, respectively. Otherwise, the remaining fraction cover is distributed to shrub and grass PFT using a 1 km ratio data derived from the GLC_FCS30D product. This data is calculated as the ratio of shrub to grass LCT within 1×1km windows.

3. The leaf types (broadleaf and needleleaf) and phenology were assigned to tree and shrub PFTs if the GLC_FCS30D product had this information on the LCT legend, after which there would be four types of tree PFTs and two types of shrub PFTs. Otherwise, the leaf types and phenology of the PFTs were assigned based on 1 km fractional data derived from the GLC_FCS30D product, calculated as the relative proportions of different leaf types and phenological classes of LCTs within 1×1 km windows. In rare cases where LCT fractions could not be determined due to the absence of an explicit legend type, a climate zone-based look-up table derived from the GLC_FCS30D and Köppen-Geiger climate zone products was applied to determine the leaf type and phenology fractions of tree and shrub PFTs.

4. The photosynthetic pathway (C3, C4) of grasses was determined based on the fraction of herbaceous vegetation, climatology monthly precipitation and temperature from WorldClim Version2, and grass PFT LAI (Sect. 2.2.2), following the method of Still et al. (2003).

5. The Köppen-Geiger climate zone product was used to assign climate zone classifications to PFTs following the method of Poulter et al. (2011).

https://doi.org/10.5194/essd-2026-21
Preprint. Discussion started: 9 February 2026

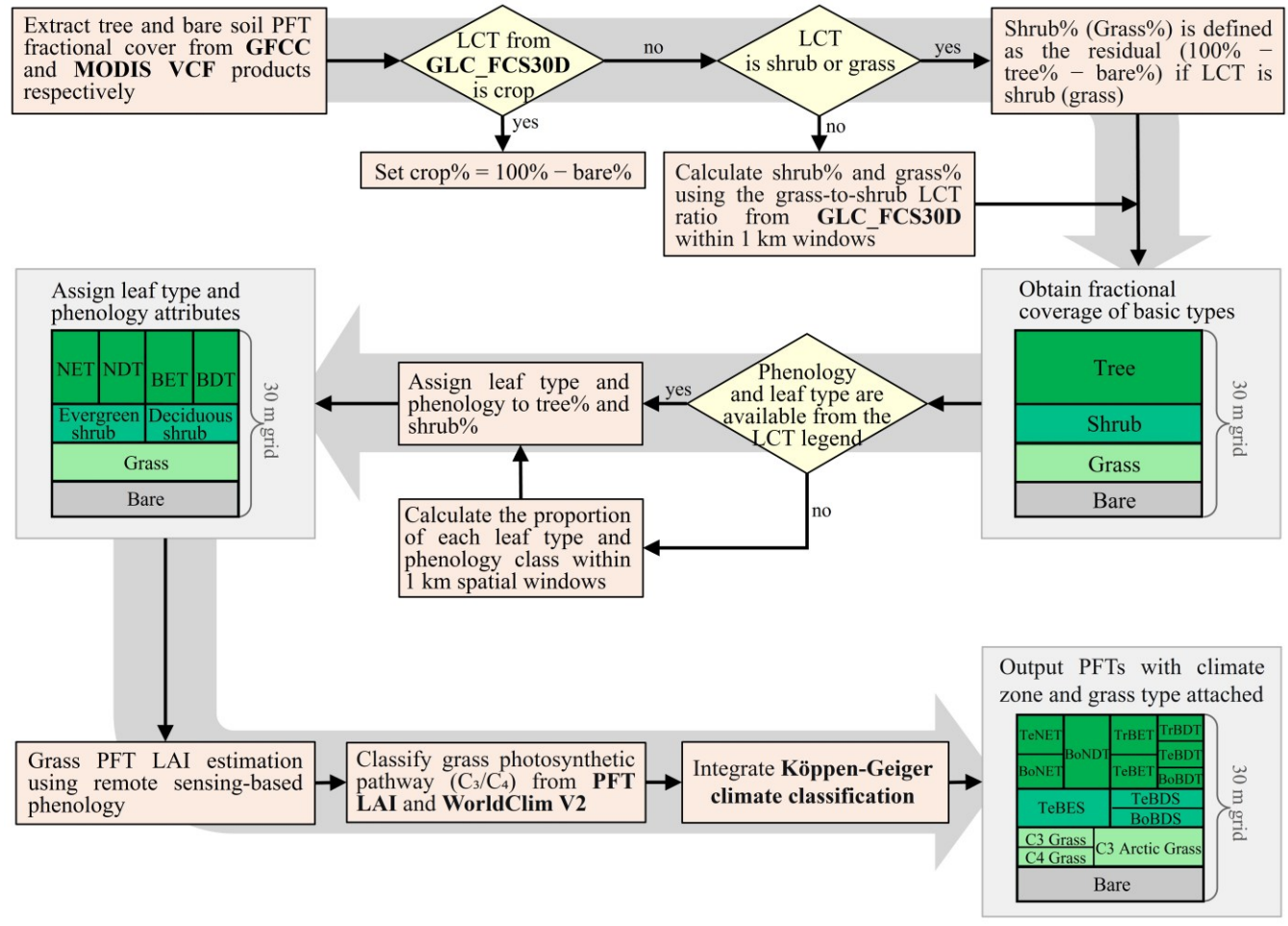

Figure 1: Flowchart of the 30 m plant functional type（PFT) mapping workflow.

For the period prior to 2000, PFT data were derived following the approach of Harper et al. (2023) to handle grids with dynamic land cover changes, due to the limited availability of ancillary datasets. The main strategy is to assign PFT attributes to grids experiencing land cover transitions by referencing neighboring static grids. Specifically, static grids (30 m grids whose LCT remained unchanged from 1985 to 2022) were first identified based on the GLC_FCS30D land cover product. A look-up table was then generated within each 0.25° window to link LCT classes with the corresponding PFT fractional cover, based on the PFT distribution for the reference year 2000 and the grid's own LCT. For dynamic grids, PFT composition was determined using the grid's LCT and this look-up table, enabling the generation of PFT fractional cover data for 1985, 1990, and 1995. The final map includes 16 PFTs and four non-vegetated types (Table 2). The fractional cover of non-vegetated types was assigned as either 0% or 100% based on the GLC_FCS30D product.

https://doi.org/10.5194/essd-2026-21
Preprint. Discussion started: 9 February 2026

Table 2. PFT classification of the PFT30 dataset.

PFTs	Other types
Bare Soil	Urban
Temperate Needleleaf Evergreen Tree (TeNET)	Wetland
Boreal Needleleaf Evergreen Tree (BoNET)	Waterbody
Boreal Needleleaf Deciduous Tree (BoNDT)	Permanent ice and snow
Tropical Broadleaf Evergreen Tree (TrBET)	
Temperate Broadleaf Evergreen Tree (TeBET)	
Tropical Broadleaf Deciduous Tree (TrBDT)	
Temperate Broadleaf Deciduous Tree (TeBDT)	
Boreal Broadleaf Deciduous Tree (BoBDT)	
Temperate Broadleaf Evergreen Shrub (TeBES)	
Temperate Broadleaf Deciduous Shrub (TeBDS)	
Boreal Broadleaf Deciduous Shrub (BoBDS)	
C3 Arctic Grass	
C3 Grass	
C4 Grass	
Crop	

2.2.2 PFT-specific LAI and SAI calculation

The global 500 m monthly PFT LAI dataset for 1985–2020 was derived by combining remotely sensed grid-scale LAI with the PFT30 dataset. The grid LAI data was constructed by integrating the LAI4g product and the reprocessed MODIS LAI product to ensure long-term temporal continuity. Specifically, LAI4g was used for the period 1985–2003, while the reprocessed MODIS LAI was adopted thereafter. This choice was motivated by inconsistency between MOD15A2H and MCD15A2H LAI products, which are used for different periods in the reprocessed MODIS LAI dataset and may introduce artificial trends, particularly in equatorial regions (Lin et al., 2023). For preprocessing, the 1/12° LAI4g data were resampled to 500 m resolution using linear interpolation to ensure consistency with the spatial resolution of the PFT LAI dataset and aggregated from half-monthly to monthly time steps. The PFT30 dataset was updated every five years prior to 2000, and PFT distributions for intermediate years were accordingly assumed constant (e.g., the 1985 map was applied to 1985–1989). Based on the harmonized grid LAI and PFT30 datasets, grids with a PFT fraction exceeding 80% were identified, and their grid LAI values were treated as representative of the corresponding PFT. These PFT-level values were then used as weights to distribute the grid LAI among different PFTs. The procedure is summarized as follows:

https://doi.org/10.5194/essd-2026-21
Preprint. Discussion started: 9 February 2026

1. For each PFT whose fractional cover exceeds 80% within 500 m grids, the mean grid LAI is calculated within each 0.25-degree window. These mean values serve as the weighting factors for distributing grid LAI among PFTs for all 500 m grids within the corresponding 0.25-degree window.

2. In cases where no grid within a 0.25-degree window contains a PFT fraction exceeding 80%, the weighting factor for that PFT is obtained from a hemispheric look-up table, constructed by calculating the mean LAI of 500 m grids with more than 80% PFT cover within each climate zone. The weighting factor is therefore assigned based on the PFT type and the climate zone to which the target grid belongs.

3. Using the weighting factors derived from the previous two steps, together with the grid LAI and the PFT fractions, the monthly PFT LAI is calculated by making full use of these remote sensing information following Eq. (1):$PFTLAI_{ipft} = \frac{Ratio_{ipft}}{\sum_{ipft=1}^{16} Ratio_{ipft} * Frac_{ipft}} \cdot GridLAI,$ (1)

where $ipft$ denotes a specific PFT, $PFTLAI_{ipft}$ is its corresponding LAI value, $GridLAI$ is the grid-scale LAI value, $Ratio_{ipft}$ is the weighting factor for each PFT, and $Frac_{ipft}$ is the PFT cover fraction aggregated from the 30 m PFT product (Section 2.2.1).

The PFT-specific stem area index (PFT SAI), which covaries with the seasonal evolution of PFT LAI, is estimated following the approaches of previous studies (Lawrence and Chase, 2007; Zeng et al., 2002). For each month, the PFT SAI is calculated as the sum of the remaining dead leaf and stem area from the previous month and the loss of green leaf area, with the final value constrained by predefined minimum PFT SAI thresholds.

3 Results

3.1 Overview of the new PFT map

3.1.1 Spatial pattern

The new PFT map has a spatial resolution of 30 m (18000 × 18000 pixels per 5° × 5° tile) and provides dynamic PFT distributions for the period 1985–2020. The classification includes 16 vegetated types and 4 other non-vegetated types including urban, water body, wetland, permanent snow and ice (Table 2). The 16 vegetated types were combined for the same lifeform from different climate zones (Fig. 2). Natural vegetation occupied over half of the land area, with 18.27% of tree cover, 18.07% of shrub cover and 16.5% of grass cover. The fraction cover of crop is 10.92% and bare cover is 20.92%. As for the non-vegetation types, there is 0.82% covered with urban, 2.27% with waterbody, 2.28% with wetland and 9.94% with permanent snow and ice.

https://doi.org/10.5194/essd-2026-21
Preprint. Discussion started: 9 February 2026

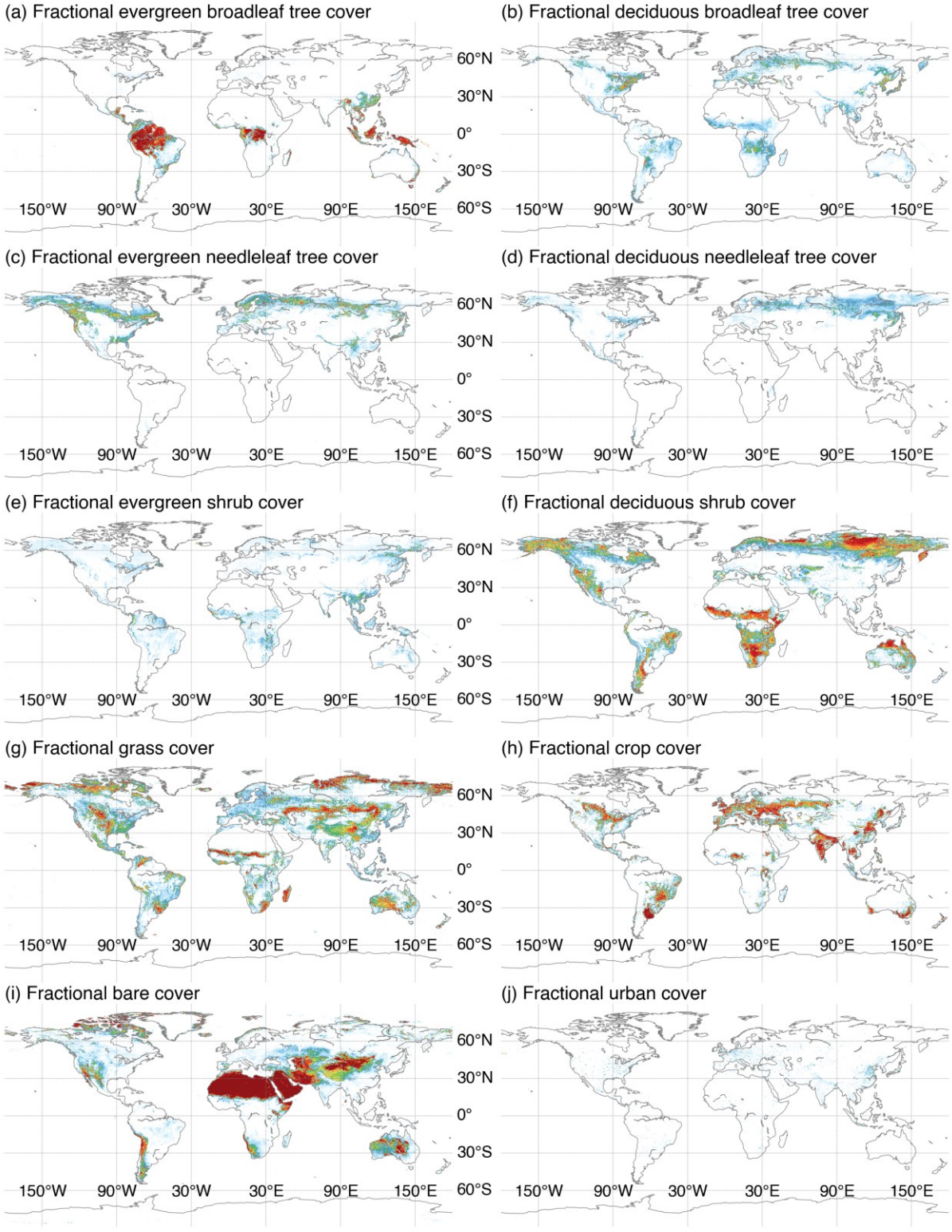

https://doi.org/10.5194/essd-2026-21
Preprint. Discussion started: 9 February 2026

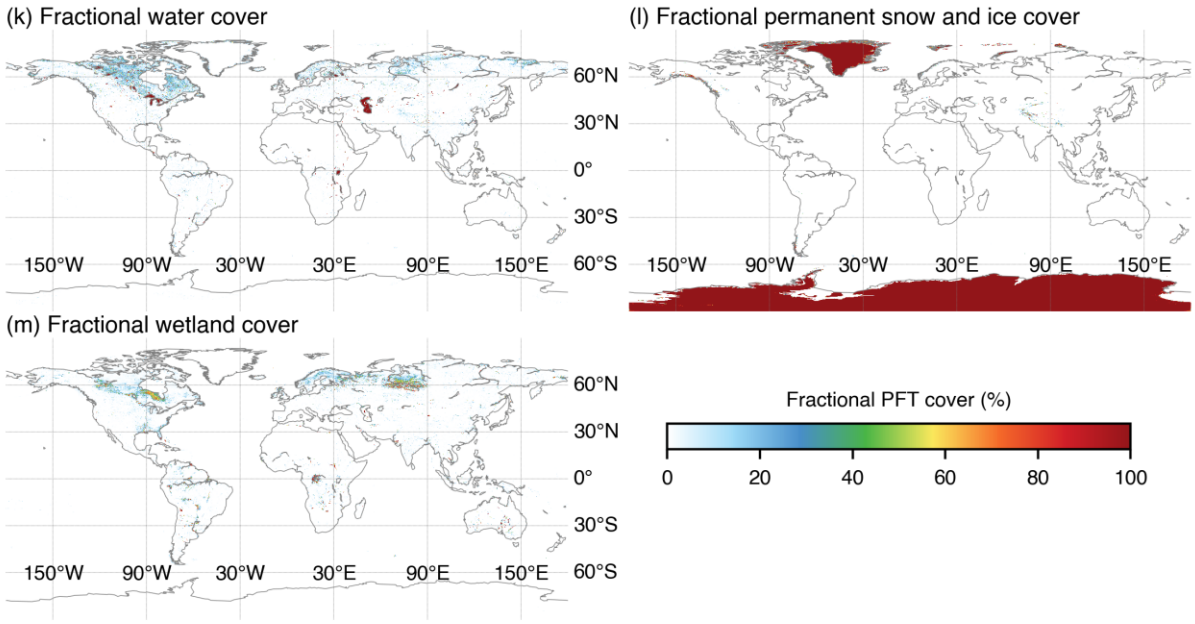

Figure 2: Distribution of PFTs and other non-vegetated land types in 2010. (a) Evergreen broadleaf tree cover fraction, including TrBET, TeBET. (b) Deciduous broadleaf tree cover fraction, including TrBDT, TeBDT, BoBDT. (c) Evergreen needleleaf tree cover fraction, including TeNET, BoNET. (d) Deciduous needleleaf tree cover fraction. (e) Evergreen shrub cover fraction. (f) Deciduous shrub cover fraction, including TeBDS and BoBDS. (g) Grassland cover fraction, including C_3 Arctic grass, C_3 non-Arctic grass and C_4 grass. (h) Cropland cover fraction. (i-m) Barren, urban, water bodies, permanent snow and ice, and wetland cover fractions.

3.1.2 Temporal variation

We investigated multi-year changes in global PFT distributions from 1985 to 2020 by aggregating PFTs with similar vegetation types and analyzing their annual variability. Figures 3a and 3b show the spatial distribution of PFT with the most significant increases and decreases in fractional cover at 0.5° resolution. Changes were classified into three categories based on the fraction of area change per grid: 1–5% as moderate change, >5% as dramatic change, and the remaining areas (white in the figures) as relatively stable. Stable areas, minimally affected by human activities and climate change, are mainly concentrated in arid regions such as the Sahara, the Middle East, and northwestern China, while most other regions experienced notable shifts in PFT composition under combined climatic and anthropogenic influences.

Tree cover declined continuously from 1985 to 2005 (Fig. 3c), especially between 1995 and 2000, with a reduction of approximately 735,370 km² due to large-scale deforestation in tropical regions and cropland expansion in the southeastern Amazon and Southeast Asia. Between 2005 and 2010, tree cover increased, primarily driven by afforestation and reforestation programs in China, as well as tree expansion in Europe, the eastern United States, and

https://doi.org/10.5194/essd-2026-21
Preprint. Discussion started: 9 February 2026


Open Access Earth System Science Data Discussions

other regions. Overall, 20.5% of land grids experienced moderate tree cover increases, and 6.7% showed dramatic increases. Due to the 5-year temporal resolution of the GFCC tree cover data, these changes appear as stepwise transitions in the time series.

Shrub and bare ground areas exhibited noticeable interannual fluctuations but generally declined. Shrub losses occurred in multiple regions, including conversion to cropland in the southern Amazon and to trees in parts of sub-Saharan Africa and eastern Siberia. In some high-latitude areas, shrubs expanded into bare ground due to rising temperatures, snow cover changes, and permafrost thaw (Myers-Smith et al., 2011), but these were minor compared to the global declining trend. Bare ground showed a considerable decreasing trend, with 17.6% of the land surface experiencing notable reductions. This decline was partly linked to cropland expansion in southwest Asia and increases in shrub and grassland cover. In addition, in regions such as northern China, sub-Saharan Africa, and polar margins, large areas of bare ground were converted to grasslands, resulting in a net increase in grassland area over the period.

Cropland expanded globally, driven by forest conversion in tropical regions and natural short vegetation in central South America, Southeast Asia, India, and parts of Europe, under the combined effects of agricultural expansion, population growth, and economic development. At the same time, urban areas experienced moderate growth overall, with the fastest growth occurring between 1995 and 2000, notably in eastern China. Overall, these patterns reflect a global greening trend driven by the combined influence of climate change and human activities.

https://doi.org/10.5194/essd-2026-21
Preprint. Discussion started: 9 February 2026

Open Access Earth System Science Data Discussions

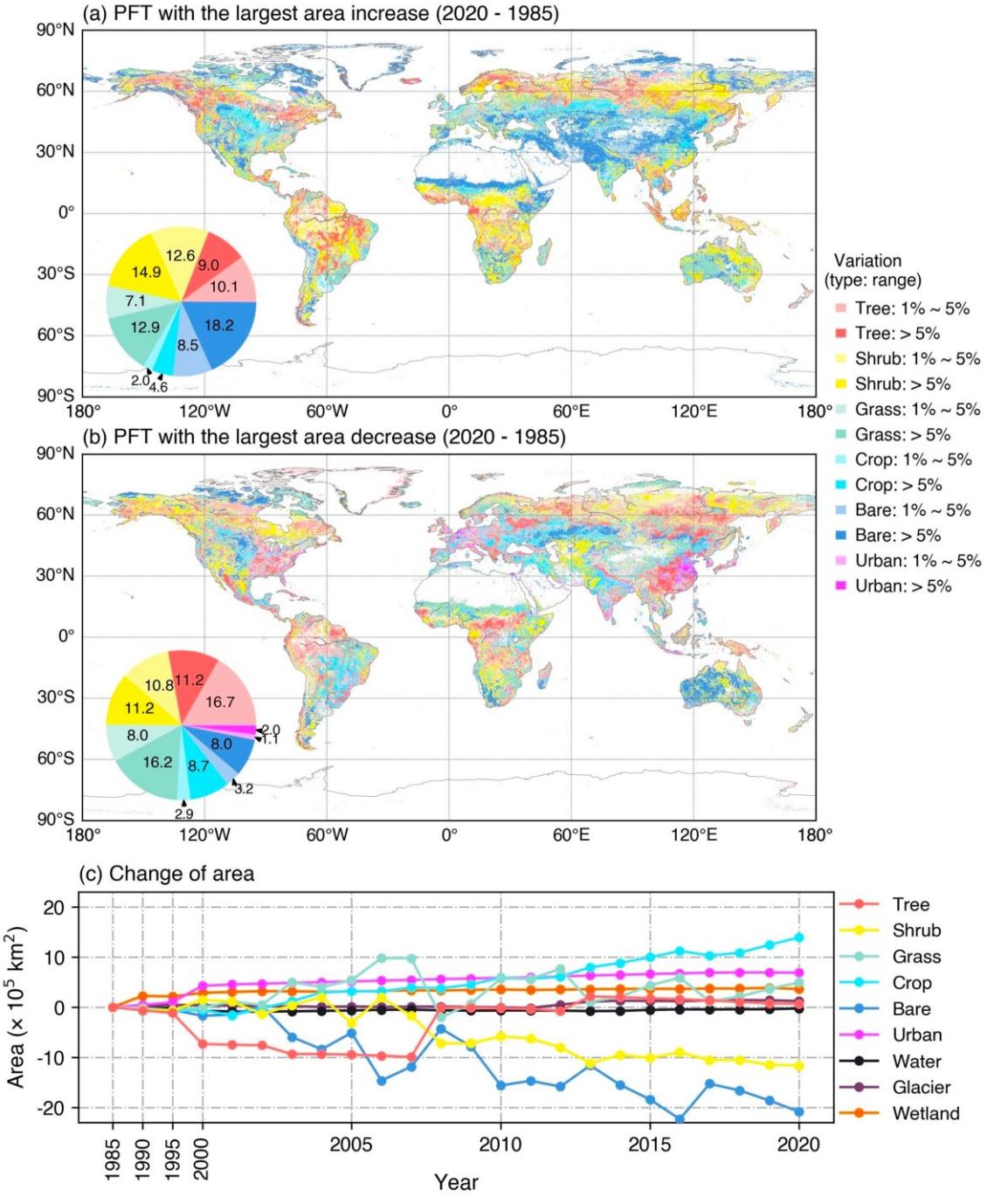

Figure 3: Fractional PFTs cover changes over the period 1985–2020. (a) PFT with the largest area increase and (b) PFT with the largest area decrease; the accompanying pie charts summarize their global land fractions. Both maps (a and b) display only grid cells at 0.5° resolution where the fractional cover change exceeds 1%. c) Time series of PFT area change.

https://doi.org/10.5194/essd-2026-21
Preprint. Discussion started: 9 February 2026

Open Access Earth System Science Data Discussions

280

3.2 Comparison and evaluation with existing data at the global scale

Three existing global PFT products were collected and compared with the newly developed PFT30 dataset. As introduced in Section 1, the ESA-CCI PFT product was generated from the 300 m LC_CCI land cover map using a cross-walking approach that allocates fixed PFT compositions to land cover classes, and therefore lacks explicit representation of subgrid spatial
285 heterogeneity (Poulter et al., 2015). The updated global PFT dataset developed by Harper et al. (2023), covering the period 1992–2020, was produced through a systematic workflow that integrates multiple high-resolution datasets to assign vegetation life form, phenology and abiotic land types. In addition, the Common Land Model version 2024 (CoLM 2024) (Dai et al., 2003) provides a global 500 m PFT dataset for the period 2000–2020. This dataset was generated by combining several satellite products, including MODIS VCF to determine the fractional cover of trees, non-tree vegetation and bare soil; AVHRR VCF
290 to distinguish tree types; and the ESA LC_CCI land cover product with its cross-walking table to get the fraction of different non-tree vegetation types. Hereafter, these three datasets are referred to as ESA_{global}, ESA_{local} and CoLM, respectively.

The four products are similar in the fraction of tree cover and bare soil cover, while the difference in short vegetation fraction is more pronounced, which may be because there are few direct observations on both shrub and grass cover. The fraction cover of the vegetated type of the new data lies between the other three products, despite the fraction of shrub
295 cover being slightly higher than that of CoLM. Compared with the other three products, ESA_{local} shows a markedly different representation of natural short vegetation, characterized by the lowest shrub cover and the highest grass cover fraction. The low shrub coverage may be related to the assumption that shrub PFTs only occur within shrub land cover types. Combined with the assumption that bare soil exists only in sparsely vegetated land cover types, this may result in the most grass coverage. In addition, the new data shows the highest urban coverage, which may be attributed to the
300 finer 30 m land cover data that better captures rural built-up areas around cities.

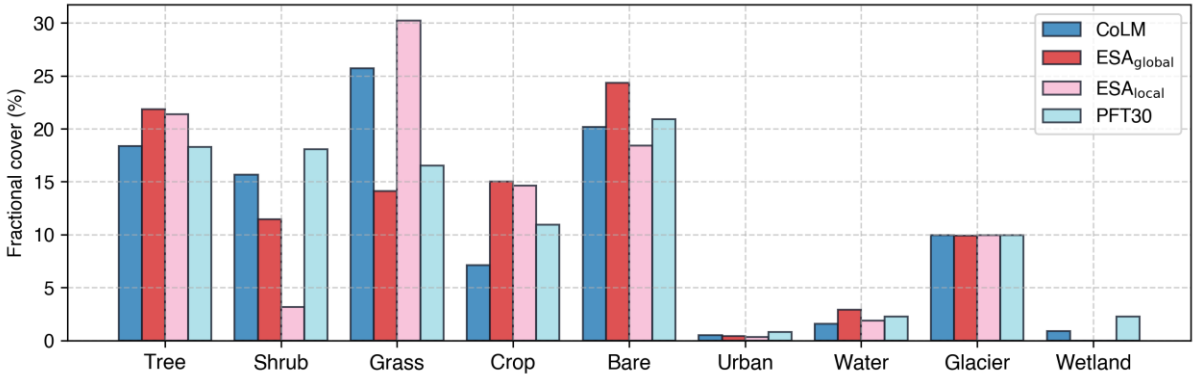

Figure 4: Comparison of global PFTs land fractional cover in 2010 across four different products.

https://doi.org/10.5194/essd-2026-21
Preprint. Discussion started: 9 February 2026


Open Access Earth System Science Data Discussions

The differences in dominant PFT distributions between PFT30 and three other products at 0.05° resolution for 2010 are shown in Fig. 5, with the largest discrepancies observed for shrub and grass PFTs. For example, in central and southern Africa, PFT30 reveals a more extensive distribution of deciduous shrub-dominated areas, whereas CoLM and ESA_{local} primarily exhibit grassland coverage. Furthermore, in western and central Australia, CoLM shows the largest spatial extent of grasslands, followed by the PFT30 and $ESA_{local,}$ with ESA_{global} having the smallest (dominated by bare soil). This pattern reflects substantial uncertainty in the discrimination between shrub and grass. In contrast, discrepancies in bare soil distribution are relatively minor. However, in southwestern Asia, ESA_{local} identifies a substantially smaller area dominated by bare soil, likely due to its underlying assumption that bare soil exists primarily within the "Sparse vegetation" or "Bare areas" LCTs.

Tree PFTs are mainly distributed in tropical regions and the mid-to-high latitudes of the Northern Hemisphere, showing broadly consistent spatial patterns across the compared products. An exception is observed in ESA_{global}, which exhibits the highest fraction of deciduous needleleaf PFTs over northeastern Asia. This discrepancy is likely attributable to the use of a globally uniform look-up table for assigning tree PFT fractions, which may limit the representation of regional spatial heterogeneity. Although ESA_{global} and ESA_{local} are derived from the same land-cover base map, ESA_{local} is dominated by grassland in this region, highlighting inconsistencies between rule-based cross-walking approaches and ancillary-data-driven PFT estimates. Also in this region, PFT30 shows a distribution pattern similar to that of CoLM, both being dominated by deciduous-shrub PFTs, whereas ESA_{local} primarily represents grassland. This again highlights the uncertainty in distinguishing shrub and grass PFTs among current global PFT datasets. While the overall distribution of tree PFTs appears broadly consistent across products, notable differences persist in the identification and classification of specific tree PFTs. In northwestern Eurasia, the CoLM dataset represents tree PFTs solely as evergreen needleleaf types, while the new dataset depicts a mixture of evergreen needleleaf, deciduous broadleaf, and deciduous needleleaf PFTs. In contrast, the ESA_{global} and ESA_{local} products show a combination of evergreen needleleaf and deciduous broadleaf PFTs.

https://doi.org/10.5194/essd-2026-21
Preprint. Discussion started: 9 February 2026

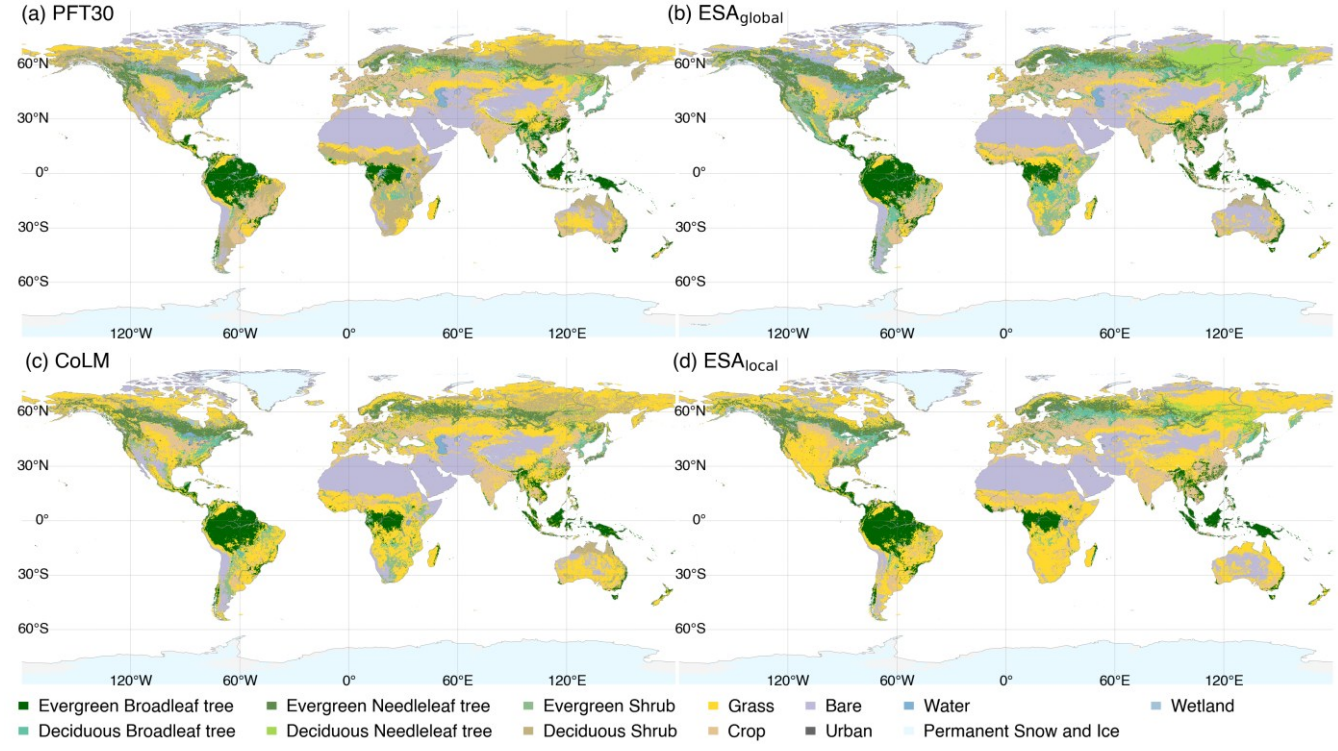

Figure 5: Distribution of dominant PFT in 0.05° grids of four PFT datasets in 2010.

3.3 Validation of PFT datasets

The PFT30 dataset and three other existing products were validated using a independent flux tower site attribute dataset (Shi et al., 2024), which compiles information from site descriptions in the literature, regional networks, and FLUXNET BADM files. Fractional PFT cover data were available for 53 sites (Fig. 6).

https://doi.org/10.5194/essd-2026-21
Preprint. Discussion started: 9 February 2026

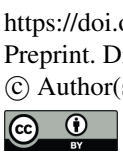

Open Access Earth System Science Data Discussions

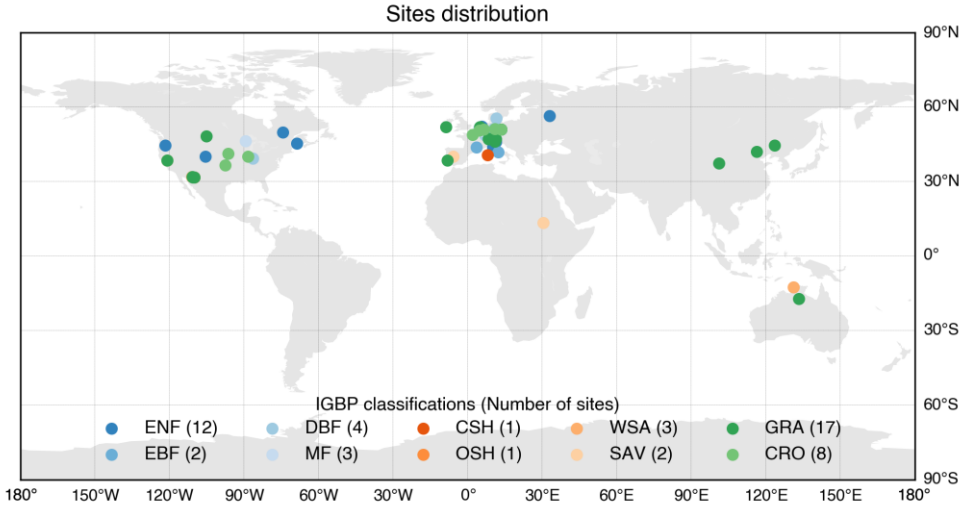

Figure 6: Distribution of sites used for PFT data validation.

335 The fractional PFT data were aggregated into three categories, namely tree, short vegetation, and bare soil. The number of bare soil samples was smaller than that of vegetated types because most sites are fully vegetated. The results indicate that PFT30 achieved the highest correlations and the lowest RMSE among the four products for both tree and short vegetation fractional cover (Fig. 7). Moreover, PFT30 and CoLM exhibited higher correlations and lower biases in bare soil fractional cover than the other two products. This relatively consistent performance is likely attributable their shared use of the MODIS VCF dataset
340 as a primary data source. For short vegetation, ESA_{global} showed a relatively low correlation coefficient ($R = 0.57$), along with larger RMSE and mean bias compared with the other products, which likely reflects the limited capacity of the look-up table approach to represent land surface heterogeneity. ESA_{local} also exhibited weaker performance in short vegetation validation, potentially because it assumed shrub PFTs occur only within shrub LCTs, thereby neglecting shrub fractions embedded in other LCTs. In contrast, by deriving vegetation composition from 30 m high-resolution remote-sensing data, PFT30 achieved
345 better validation performance at the 500 m scale.

https://doi.org/10.5194/essd-2026-21
Preprint. Discussion started: 9 February 2026

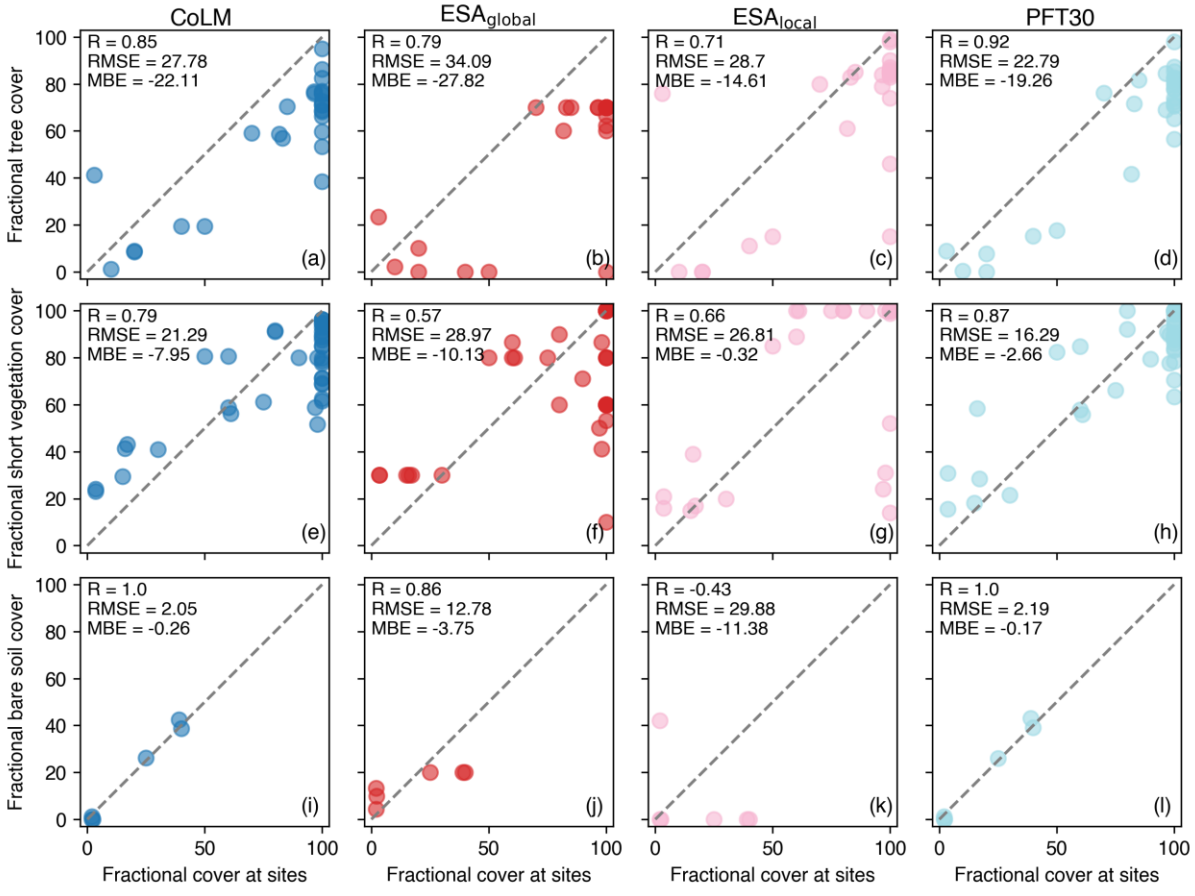

Figure 7: Site-scale validation of four global PFT mapping products (columns show CoLM, ESA_{global}, ESA_{local} and PFT30 respectively). Each row represents the fraction of tree cover, short vegetation cover and bare soil cover respectively.

350

3.4 Comparison of PFT LAI data from the remote-sensing phenology scheme and the empirical phenology scheme

The PFT LAI data produced by the remote-sensing phenology scheme was compared with that produced by the empirical phenology scheme used in the CLM model (Lawrence and Chase, 2007) to quantify the differences arising from the two methods, at both the grid and global scales. A representative 500 m grid cell dominated by mixed PFTs (temperate deciduous
355 broadleaf shrubs, C_3 non-arctic grass, and crops) in 2005 was selected to illustrate the characteristics of LAI allocation under the two schemes (Fig. 8). The allocation weight ratio of different PFTs against that of the grassland PFT remains unchanged in the empirical phenology scheme due to its uniform rules. This approach fails to adequately capture the distinct seasonal dynamics of different vegetation types at fine spatial scales. In contrast, the new scheme enhances the differentiation of growth patterns among PFTs by incorporating observed LAI dynamics from remote sensing. The allocation weight ratio of crops to

https://doi.org/10.5194/essd-2026-21
Preprint. Discussion started: 9 February 2026

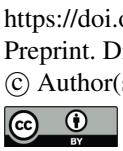

360 grass exhibits pronounced seasonal variation throughout the year: the ratio reaches its lowest value in April, being only 0.7 times that of grass, indicating that crops are still in early growth stages while grass has already established considerable cover; by August, the ratio peaks at 2.4 times that of grass, reflecting the rapid growth of crops during the peak season. However, such dynamic interactions between crop and grass PFT LAI cannot be captured by the empirical phenology scheme.

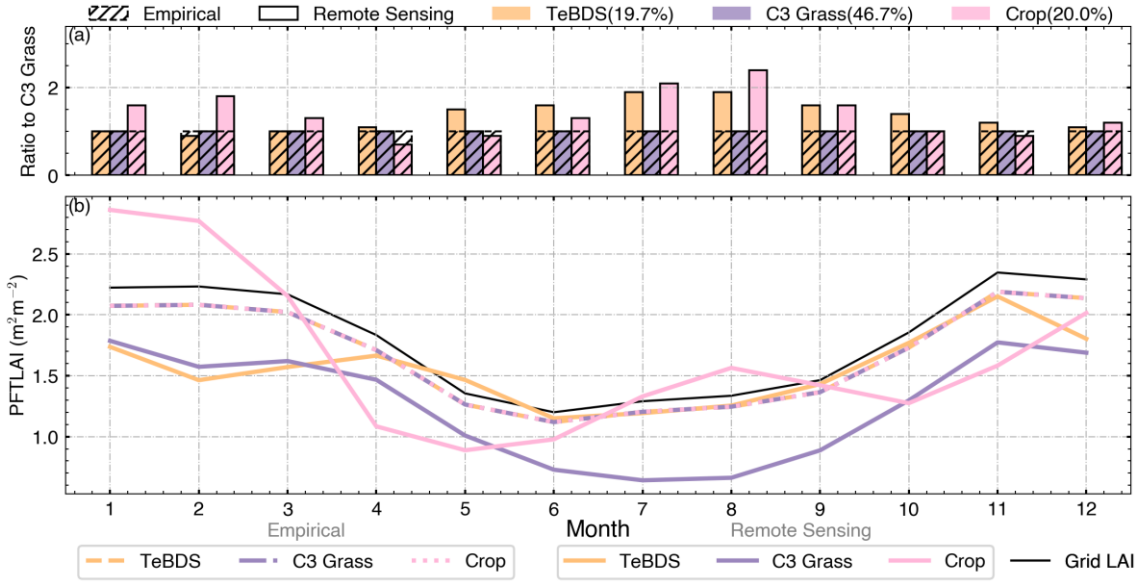

365 **Figure 8: Comparison of remote sensing-based phenology and empirical phenology schemes for PFT LAI in a 500-meter grid (25.027°S, 50.098°W) with mixed natural vegetation and crops. (a) Ratio of assigned weights for each PFT relative to C_3 grass; (b) Time series of PFT LAI and grid-scale LAI. Descriptions of PFT abbreviations are provided in Table 2.**

For the global-scale comparison, the PFT LAI data were aggregated into five major PFT types: evergreen tree, deciduous tree,
370 shrub, grass and crop. The most pronounced differences occur in regions dominated by deciduous trees (Fig. 9), such as eastern North America and northwestern Asia, where PFT LAI values increase under the new scheme. The largest increase in deciduous tree PFT LAI occurs in summer, accompanied by a corresponding decrease in shrub and grass PFT LAI. In southern China, the evergreen tree PFT LAI derived from the new scheme is slightly lower than that from the empirical phenology scheme during summer but higher in winter, thereby reducing the overall seasonal amplitude. However, in the mid-to-high
375 latitudes of the Northern Hemisphere, the seasonal variation of evergreen tree PFT LAI resembles that of deciduous trees, with the most pronounced increase occurring in summer. This is likely because remote sensing observations in these regions are affected by snow cover, which limits the accurate retrieval of evergreen tree phenological characteristics from satellite data.

In crop-dominated regions such as areas south of the Amazon and western Europe, the differences in crop PFT LAI between the two schemes vary seasonally. Compared with the empirical phenology scheme, the new scheme shows higher crop PFT
380 LAI in western Europe during winter, but relatively lower values in summer. This adjustment refines the seasonal dynamics

https://doi.org/10.5194/essd-2026-21
Preprint. Discussion started: 9 February 2026

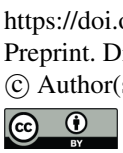

of crop PFT LAI and avoids the equal-weight allocation of LAI between grassland and cropland in the empirical phenology approach, thereby accounting for the influence of human management practices on crop PFT LAI. Overall, the primary differences between the two schemes are manifested in the redistribution of grid-scale LAI among PFTs, including increases in deciduous tree PFT LAI with corresponding reductions in shrub PFT LAI, as well as adjustments to the seasonal variation
385 patterns of evergreen tree and crop PFT LAI.

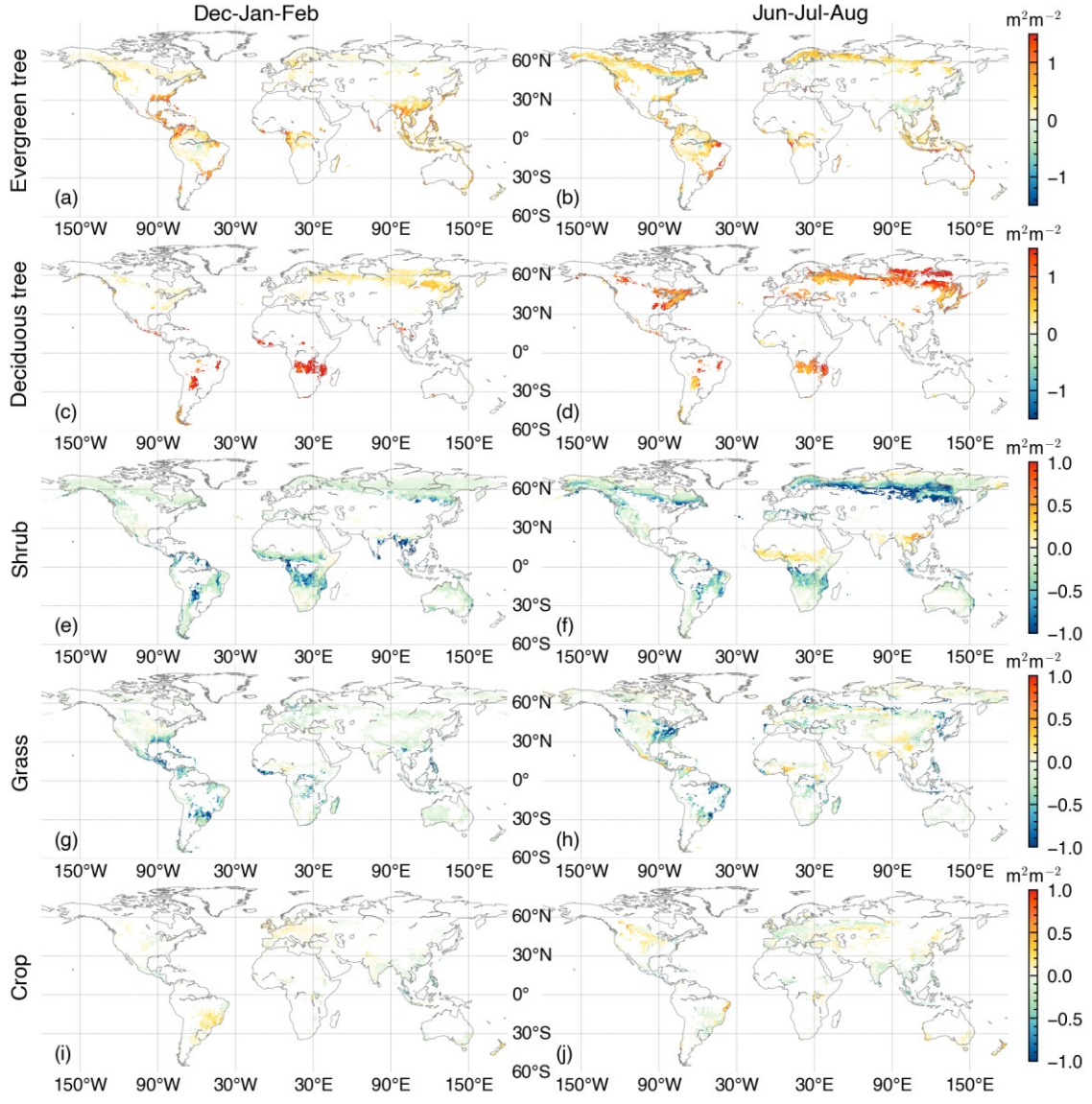

Figure 9: Difference in PFT LAI between the remote-sensing phenology scheme and the empirical phenology scheme.

https://doi.org/10.5194/essd-2026-21
Preprint. Discussion started: 9 February 2026

3.5 Comparison of PFT- and LCT- based analysis on Amazon rainforest dynamic change

Traditional land cover analyses often rely on LCT products, which do not always effectively reveal realistic vegetation changes. In this study, we evaluated vegetation variations in selected subregions of the Amazon rainforest during 2005–2015 as a demonstration, using multiple datasets including LAI, PFT, PFT LAI, and LCT at 0.5° resolution. Variation in PFT and PFT LAI were derived from the newly developed datasets in this study. Changes in LAI were derived from the reprocessed MODIS C6.1 LAI product, which indicates a greening signal along parts of the Amazon River basin (Fig. 10), and were used as a reference to assess whether PFT-based and LCT-based analyses can capture these vegetation changes. The fractional cover of forest LCT was obtained by aggregating all forest-related types (10 in total) from the GLC_FCS30D product.

In region A, LAI increased by 0.31 m^2m^{-2}, whereas the forest fraction derived from LCT data decreased by 0.79%, suggesting that analyses based solely on LCT may provide inadequate or even misleading interpretations of vegetation dynamics. In contrast, PFT LAI data show that tree PFT LAI increased by 0.33 m^2m^{-2}, indicating that the observed greening is mainly associated with enhanced canopy density of tree PFTs. Similarly, in region B, an LAI increase of 0.17 m^2m^{-2} cannot be explained by LCT-based analysis alone, as the forest fraction decreased by 0.60%. In contrast, PFT-based results reveal that the tree fraction increased by 1.84%, accompanied by a 0.09 m^2m^{-2} increase in tree PFT LAI, indicating that changes in both PFT fraction and PFT LAI contribute to the observed greening signal.

This discrepancy may arise because PFT fraction data are more sensitive to subtle land surface changes than traditional LCT products, as PFT transitions do not necessarily lead to detectable LCT changes. For example, in regions C and D, the fraction of forest types remains nearly unchanged in LCT data, whereas PFT results reveal a continuous increase in the tree fraction. Consequently, by combining PFT and LAI information, PFT LAI can better capture both interannual and seasonal variations in vegetation, indicating a stronger capability for vegetation dynamics analysis than LCT-based approaches.

https://doi.org/10.5194/essd-2026-21
Preprint. Discussion started: 9 February 2026

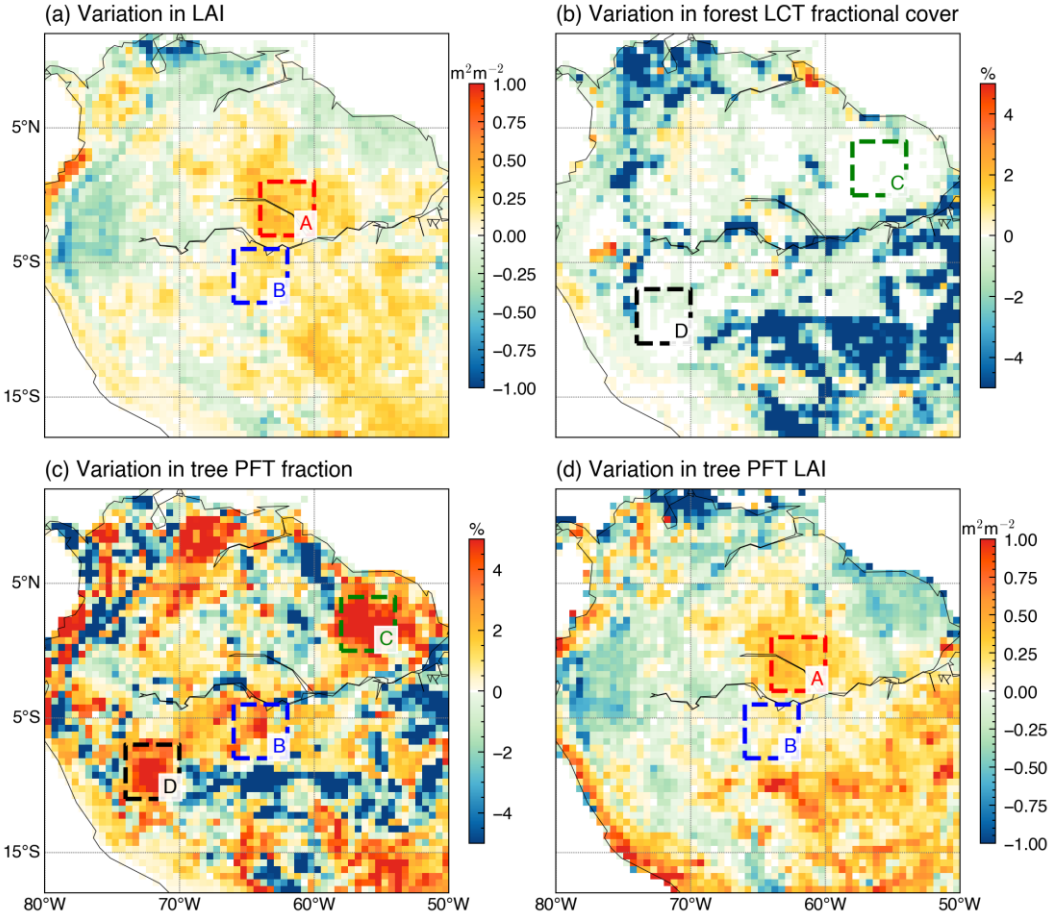

Figure 10: Vegetation dynamics evaluation through differences in several variables (2015−2005). (a) LAI; (b) LCT; (c) PFT; (d) PFT LAI.

4 Data availability

The PFT30 dataset at 30 m and 500 m resolution, together with the corresponding 500 m PFT LAI and PFT SAI products, is provided in NetCDF format at a spatial tiling of 5° × 5°. The data are further packaged into global archives subdivided into 30° × 30° tiles and distributed as tar files. Access to the PFT30 datasets is provided via https://doi.org/10.5281/zenodo.18139027 (Lin and Yuan, 2026a). Access to the PFT LAI and PFT SAI products is provided via https://doi.org/10.5281/zenodo.18113489 (Lin and Yuan, 2026b)

https://doi.org/10.5194/essd-2026-21
Preprint. Discussion started: 9 February 2026

5 Conclusions

This study derived a global 30 m PFT dataset (PFT30) and a corresponding 500 m PFT LAI product for 1985–2020, both updated annually, with the exception that PFT30 prior to 2000 was updated at five-year intervals. This dataset reduces PFT compositional uncertainty within model grid cells by integrating multiple high-resolution remote sensing products, providing more accurate subgrid heterogeneity representation than existing global datasets. In parallel, the PFT LAI product captures realistic phenological variations by making use of remote sensing information, overcoming the limitations of empirical approaches commonly used. This observational constraint ensures physically consistent LAI evolution across different vegetation types.

The PFT30 dataset reliably captures PFT area changes that align with previous studies, notably increases in tree cover from reforestation/afforestation and a widespread greening trend coupled with bare soil reduction. Compared with three other hundred-meter-resolution global PFT products, PFT30 achieves better performance in site-scale validation, owing to the integration of high-resolution ancillary datasets. Furthermore, differences in PFT LAI between our remote-sensing-based phenology scheme and conventional empirical phenology schemes occur mainly in the discrimination of short vegetation types, including (shrubs, grasslands and crops). By incorporating direct remote sensing information, our approach better captures realistic vegetation phenological dynamics and agricultural management signals. Assessments in selected subregions of the Amazon rainforest further highlight the advantages of PFT-based analysis, where the use of PFT fractional cover and PFT LAI data better captures vegetation dynamics compared with traditional LCT-based methods relying on LCT products.

This finer resolution land surface dataset offers several advantages. First, it enables improved fine-scale land surface and climate modeling from regional to global scales. Second, its long-term coverage facilitates quantification of historical land use and land cover change impacts. Combining PFT and PFT LAI information provides enhanced capability for vegetation dynamics analysis and modeling compared to land cover type change detection alone. Third, by incorporating observational constraints from multiple high-resolution remote-sensing products, it provides a robust benchmark of vegetation structure for evaluating dynamic vegetation models.

Author contributions

HY conceived the research. WL conducted data production and evaluation and wrote the first draft of the manuscript. WL, HY, WD, ZL and YD contributed to manuscript revision. JX, XY, SZ and ZW reviewed the data and evaluated it in land surface models, and joined the discussion of the research.

Competing interests

The contact author has declared that none of the authors has any competing interests.

https://doi.org/10.5194/essd-2026-21
Preprint. Discussion started: 9 February 2026

Open Access Earth System Science Data Discussions

Acknowledgements

We gratefully acknowledge the providers of the remote sensing and ancillary datasets used in this study. We thank the GLC_FCS30D land cover product team for providing the dataset and for their helpful responses to our data-related inquiries. The GFCC tree cover dataset provided essential high-resolution land surface information. We thank the MODIS Vegetation Continuous Fields product for subgrid fraction estimates, and acknowledge the GIMMS LAI4g dataset for its long-term global LAI record. Climate background data were obtained from the Köppen–Geiger climate classification maps and the WorldClim Version 2 global climate surfaces.

References

Beck, H. E., Zimmermann, N. E., McVicar, T. R., Vergopolan, N., Berg, A., and Wood, E. F.: Present and future Köppen-Geiger climate classification maps at 1-km resolution, Sci. Data, 5, 180214, https://doi.org/10.1038/sdata.2018.214, 2018.

Betts, R. A.: Offset of the potential carbon sink from boreal forestation by decreases in surface albedo, Nature, 408, 187–190, https://doi.org/10.1038/35041545, 2000.

Bonan, G. B., Levis, S., Kergoat, L., and Oleson, K. W.: Landscapes as patches of plant functional types: An integrating concept for climate and ecosystem models, Glob. Biogeochem. Cycles, 16, 5-1-5–23, https://doi.org/10.1029/2000GB001360, 2002.

Boysen, L. R., Brovkin, V., Arora, V. K., Cadule, P., de Noblet-Ducoudré, N., Kato, E., Pongratz, J., and Gayler, V.: Global and regional effects of land-use change on climate in 21st century simulations with interactive carbon cycle, Earth Syst. Dyn., 5, 309–319, https://doi.org/10.5194/esd-5-309-2014, 2014.

Cao, S., Li, M., Zhu, Z., Zha, J., Zhao, W., Duanmu, Z., Chen, J., Zheng, Y., and Chen, Y.: Spatiotemporally consistent global dataset of the GIMMS Leaf Area Index (GIMMS LAI4g) from 1982 to 2020, Earth Syst. Sci. Data Discuss., 1–31, https://doi.org/10.5194/essd-2023-68, 2023.

Chen, C., Park, T., Wang, X., Piao, S., Xu, B., Chaturvedi, R. K., Fuchs, R., Brovkin, V., Ciais, P., Fensholt, R., Tømmervik, H., Bala, G., Zhu, Z., Nemani, R. R., and Myneni, R. B.: China and India lead in greening of the world through land-use management, Nat. Sustain., 2, 122–129, https://doi.org/10.1038/s41893-019-0220-7, 2019.

Dai, Y., Zeng, X., Dickinson, R. E., Baker, I., Bonan, G. B., Bosilovich, M. G., Denning, A. S., Dirmeyer, P. A., Houser, P. R., Niu, G., Oleson, K. W., Schlosser, C. A., and Yang, Z.-L.: The common land model, Bull. Am. Meteorol. Soc., 84, 1013–1024, https://doi.org/10.1175/BAMS-84-8-1013, 2003.

DiMiceli, C., Carroll, M., Sohlberg, R., Kim, D.-H., Kelly, M., and Townshend, J.: MOD44B MODIS/terra vegetation continuous fields yearly L3 global 250m SIN grid V006, https://doi.org/10.5067/MODIS/MOD44B.006, 2015.

Faroux, S., Kaptué Tchuenté, A. T., Roujean, J.-L., Masson, V., Martin, E., and Le Moigne, P.: ECOCLIMAP-II/Europe: a twofold database of ecosystems and surface parameters at 1 km resolution based on satellite information for use in land surface, meteorological and climate models, Geosci. Model Dev., 6, 563–582, https://doi.org/10.5194/gmd-6-563-2013, 2013.

https://doi.org/10.5194/essd-2026-21
Preprint. Discussion started: 9 February 2026

Fick, S. E. and Hijmans, R. J.: WorldClim 2: new 1-km spatial resolution climate surfaces for global land areas, Int. J. Climatol., 37, 4302–4315, https://doi.org/10.1002/joc.5086, 2017.

Fisher, R. A. and Koven, C. D.: Perspectives on the Future of Land Surface Models and the Challenges of Representing Complex Terrestrial Systems, J. Adv. Model. Earth Syst., 12, e2018MS001453, https://doi.org/10.1029/2018MS001453, 2020.

Friedl, M. and Sulla-Menashe, D.: MODIS/terra+aqua land cover type yearly L3 global 500m SIN grid V061, https://doi.org/10.5067/MODIS/MCD12Q1.061, 2022.

Harper, K. L., Lamarche, C., Hartley, A., Peylin, P., Ottlé, C., Bastrikov, V., San Martín, R., Bohnenstengel, S. I., Kirches, G., Boettcher, M., Shevchuk, R., Brockmann, C., and Defourny, P.: A 29-year time series of annual 300 m resolution plant-functional-type maps for climate models, Earth Syst. Sci. Data, 15, 1465–1499, https://doi.org/10.5194/essd-15-1465-2023, 2023.

Hartley, A. J., MacBean, N., Georgievski, G., and Bontemps, S.: Uncertainty in plant functional type distributions and its impact on land surface models, Remote Sens. Environ., 203, 71–89, https://doi.org/10.1016/j.rse.2017.07.037, 2017.

Houldcroft, C. J., Grey, W. M. F., Barnsley, M., Taylor, C. M., Los, S. O., and North, P. R. J.: New Vegetation Albedo Parameters and Global Fields of Soil Background Albedo Derived from MODIS for Use in a Climate Model, J. Hydrometeorol., 10, 183–198, https://doi.org/10.1175/2008JHM1021.1, 2009.

IPCC: Climate Change and Land: IPCC Special Report on Climate Change, Desertification, Land Degradation, Sustainable Land Management, Food Security, and Greenhouse Gas Fluxes in Terrestrial Ecosystems, 1st ed., Cambridge University Press, Cambridge, https://doi.org/10.1017/9781009157988, 2022.

Jian, X., Zhang, X., Liu, X., Chen, K., Huang, T., Tao, S., Liu, J., Gao, H., Zhao, Y., Zhugu, R., and Ma, J.: Highly resolved satellite-remote-sensing-based land-use-change inventory yields weaker surface-albedo-induced global cooling, Atmospheric Chem. Phys., 25, 4251–4268, https://doi.org/10.5194/acp-25-4251-2025, 2025.

Ke, Y., Leung, L. R., Huang, M., Coleman, A. M., Li, H., and Wigmosta, M. S.: Development of high resolution land surface parameters for the Community Land Model, Geosci. Model Dev., 5, 1341–1362, https://doi.org/10.5194/gmd-5-1341-2012, 2012.

Lawrence, P. J. and Chase, T. N.: Representing a new MODIS consistent land surface in the Community Land Model (CLM 3.0), J. Geophys. Res. Biogeosciences, 112, G01023, https://doi.org/10.1029/2006JG000168, 2007.

Li, L., Bisht, G., Hao, D., and Leung, L. R.: Global 1 km land surface parameters for kilometer-scale Earth system modeling, Earth Syst. Sci. Data, 16, 2007–2032, https://doi.org/10.5194/essd-16-2007-2024, 2024.

Lin, W. and Yuan, H.: Finer-resolution long-term mapping of plant functional types at 30-m and 500-m resolution for Earth system modeling, https://doi.org/10.5281/zenodo.18139027, 2026a.

Lin, W. and Yuan, H.: Finer-resolution long-term plant functional types-specific leaf area index at 500-m resolution for Earth system modeling, https://doi.org/10.5281/zenodo.18113489, 2026b.

Lin, W., Yuan, H., Dong, W., Zhang, S., Liu, S., Wei, N., Lu, X., Wei, Z., Hu, Y., and Dai, Y.: Reprocessed MODIS Version 6.1 Leaf Area Index Dataset and Its Evaluation for Land Surface and Climate Modeling, Remote Sens., 15, 1780, https://doi.org/10.3390/rs15071780, 2023.

https://doi.org/10.5194/essd-2026-21
Preprint. Discussion started: 9 February 2026

Malle, J. T., Mazzotti, G., Karger, D. N., and Jonas, T.: Regionally optimized high-resolution input datasets enhance the representation of snow cover in CLM5, Earth Syst. Dyn., 15, 1073–1115, https://doi.org/10.5194/esd-15-1073-2024, 2024.

Myers-Smith, I. H., Forbes, B. C., Wilmking, M., Hallinger, M., Lantz, T., Blok, D., Tape, K. D., Macias-Fauria, M., Sass-Klaassen, U., Lévesque, E., Boudreau, S., Ropars, P., Hermanutz, L., Trant, A., Collier, L. S., Weijers, S., Rozema, J., Rayback, S. A., Schmidt, N. M., Schaepman-Strub, G., Wipf, S., Rixen, C., Ménard, C. B., Venn, S., Goetz, S., Andreu-Hayles, L., Elmendorf, S., Ravolainen, V., Welker, J., Grogan, P., Epstein, H. E., and Hik, D. S.: Shrub expansion in tundra ecosystems: dynamics, impacts and research priorities, Environ. Res. Lett., 6, 045509, https://doi.org/10.1088/1748-9326/6/4/045509, 2011.

Myneni, R., Knyazikhin, Y., and Park, T.: MODIS/terra+aqua leaf area index/FPAR 8-day L4 global 500m SIN grid V061, https://doi.org/10.5067/MODIS/MCD15A2H.061, 2021a.

Myneni, R., Knyazikhin, Y., and Park, T.: MODIS/terra leaf area index/FPAR 8-day L4 global 500m SIN grid V061, https://doi.org/10.5067/MODIS/MOD15A2H.061, 2021b.

Poulter, B., Ciais, P., Hodson, E., Lischke, H., Maignan, F., Plummer, S., and Zimmermann, N. E.: Plant functional type mapping for earth system models, Geosci. Model Dev., 4, 993–1010, https://doi.org/10.5194/gmd-4-993-2011, 2011.

Poulter, B., MacBean, N., Hartley, A., Khlystova, I., Arino, O., Betts, R., Bontemps, S., Boettcher, M., Brockmann, C., Defourny, P., Hagemann, S., Herold, M., Kirches, G., Lamarche, C., Lederer, D., Ottlé, C., Peters, M., and Peylin, P.: Plant functional type classification for earth system models: results from the European Space Agency's Land Cover Climate Change Initiative, Geosci. Model Dev., 8, 2315–2328, https://doi.org/10.5194/gmd-8-2315-2015, 2015.

Smith, T. M., Shugart, H. H., and Woodward, F. I.: Plant Functional Types: Their Relevance to Ecosystem Properties and Global Change, Cambridge University Press, 392 pp., 1997.

Still, C. J., Berry, J. A., Collatz, G. J., and DeFries, R. S.: Global distribution of C3 and C4 vegetation: carbon cycle implications, Glob. Biogeochem. Cycles, 17, 6-1-6–14, https://doi.org/10.1029/2001GB001807, 2003.

Sulla-Menashe, D., Gray, J. M., Abercrombie, S. P., and Friedl, M. A.: Hierarchical mapping of annual global land cover 2001 to present: The MODIS Collection 6 Land Cover product, Remote Sens. Environ., 222, 183–194, https://doi.org/10.1016/j.rse.2018.12.013, 2019.

Townshend, J.: Global forest cover change (GFCC) tree cover multi-year global 30 m V003, https://doi.org/10.5067/MEASURES/GFCC/GFCC30TC.003, 2016.

Wang, L., Arora, V. K., Bartlett, P., Chan, E., and Curasi, S. R.: Mapping of ESA's Climate Change Initiative land cover data to plant functional types for use in the CLASSIC land model, Biogeosciences, 20, 2265–2282, https://doi.org/10.5194/bg-20-2265-2023, 2023.

Wiltshire, A. J., Duran Rojas, M. C., Edwards, J. M., Gedney, N., Harper, A. B., Hartley, A. J., Hendry, M. A., Robertson, E., and Smout-Day, K.: JULES-GL7: the Global Land configuration of the Joint UK Land Environment Simulator version 7.0 and 7.2, Geosci. Model Dev., 13, 483–505, https://doi.org/10.5194/gmd-13-483-2020, 2020.

Winckler, J., Reick, C. H., Bright, R. M., and Pongratz, J.: Importance of Surface Roughness for the Local Biogeophysical Effects of Deforestation, J. Geophys. Res. Atmospheres, 124, 8605–8618, https://doi.org/10.1029/2018JD030127, 2019.

Wu, T., He, Y., Yang, X., and Dai, Y.: An era of hyper-resolution land surface models: truth or dare?, Natl. Sci. Rev., 12, https://doi.org/10.1093/nsr/nwaf285, 2025.

https://doi.org/10.5194/essd-2026-21
Preprint. Discussion started: 9 February 2026

Xie, X., He, B., Guo, L., Huang, L., Hao, X., Zhang, Y., Liu, X., Tang, R., and Wang, S.: Revisiting dry season vegetation dynamics in the Amazon rainforest using different satellite vegetation datasets, Agric. For. Meteorol., 312, 108704, https://doi.org/10.1016/j.agrformet.2021.108704, 2022.

Yuan, H., Dai, Y., Xiao, Z., Ji, D., and Shangguan, W.: Reprocessing the MODIS Leaf Area Index products for land surface and climate modelling, Remote Sens. Environ., 115, 1171–1187, https://doi.org/10.1016/j.rse.2011.01.001, 2011.

Zeng, X., Shaikh, M., Dai, Y., Dickinson, R. E., and Myneni, R.: Coupling of the common land model to the NCAR community climate model, J. Clim., 15, 1832–1854, https://doi.org/10.1175/1520-0442(2002)015%253C1832:COTCLM%253E2.0.CO;2, 2002.

Zeng, Z., Piao, S., Li, L. Z. X., Wang, T., Ciais, P., Lian, X., Yang, Y., Mao, J., Shi, X., and Myneni, R. B.: Impact of Earth Greening on the Terrestrial Water Cycle, J. Clim., 31, 2633–2650, https://doi.org/10.1175/JCLI-D-17-0236.1, 2018.

Zhang, X., Zhao, T., Xu, H., Liu, W., Wang, J., Chen, X., and Liu, L.: GLC_FCS30D: the first global 30 m land-cover dynamics monitoring product with a fine classification system for the period from 1985 to 2022 generated using dense-time-series Landsat imagery and the continuous change-detection method, Earth Syst. Sci. Data, 16, 1353–1381, https://doi.org/10.5194/essd-16-1353-2024, 2024.